Dalton Transactions

Accepted Manuscript

Volume 1 | Number 1 | Jan 2013 | Pages 1–100

Dalton Transactions

An international journal of inorganic chemistry

www.rsc.org/dalton

ROYAL SOCIETY OF CHEMISTRY

This is an *Accepted Manuscript*, which has been through the Royal Society of Chemistry peer review process and has been accepted for publication.

Accepted Manuscripts are published online shortly after acceptance, before technical editing, formatting and proof reading. Using this free service, authors can make their results available to the community, in citable form, before we publish the edited article. We will replace this *Accepted Manuscript* with the edited and formatted *Advance Article* as soon as it is available.

You can find more information about *Accepted Manuscripts* in the Information for Authors.

Please note that technical editing may introduce minor changes to the text and/or graphics, which may alter content. The journal's standard Terms & Conditions and the Ethical guidelines still apply. In no event shall the Royal Society of Chemistry be held responsible for any errors or omissions in this *Accepted Manuscript* or any consequences arising from the use of any information it contains.

ROYAL SOCIETY OF CHEMISTRY

www.rsc.org/dalton

Journal Name

ARTICLE TYPE

Cite this: DOI: 10.1039/xxxxxxxxxx

Received Date
Accepted Date

DOI: 10.1039/xxxxxxxxxx

www.rsc.org/journalname

Local structure of the metal-organic perovskite dimethylammonium manganese(II) formate†

Helen D. Duncan,[a] Martin T. Dove,[a] David A. Keen,[b] and Anthony E. Phillips*[a]

We report total neutron scattering measurements on the metal-organic perovskite analogue dimethylammonium manganese(II) formate, $(CD_3)_2ND_2[Mn(DCO_2)_3]$. Reverse Monte Carlo modelling shows that, in both the disordered high-temperature and ordered low-temperature phases, the ammonium moiety forms substantially shorter hydrogen bonds ($N\cdots O = 2.4$ Å and 2.6 Å) than are visible in the average crystal structures. These bonds result from a pincer-like motion of two adjacent formate ions about the dimethylammonium ion in such a way that the framework can adjust independently to the positions of nearest-neighbour dimethylammonium ions. At low temperatures the shortest hydrogen bond is less favourable, apparently because it involves an greater distortion of the framework. Furthermore, in the high-temperature phase, in addition to the three disordered nitrogen positions expected from the average crystal structure, there appear to be also smaller probability maxima between these positions, corresponding to orientations in which the dimethylammonium is hydrogen-bonded to the two oxygen atoms of a single formate ion. The spontaneous strain across the phase transition reveals a contraction of the framework about the dimethylammonium cation, continuing as the material is cooled below the transition temperature. These results provide direct evidence of the local atomic structure of the guest-framework hydrogen bonding, and in particular the distortions of the framework, responsible for the phase transition in this system.

1 Introduction

The family of inorganic perovskites, of general formula ABX_3, displays a rich diversity both of chemical compositions and of the corresponding physical properties, including large dielectric constants, elasto-optic coupling, and electric, elastic, and magnetic ordering. As a result, perovskites currently find application as sensors, actuators, transducers, capacitors, electrodes, and data storage materials such as ferroelectric random-access memory.[1–3] It is now clear that metal-organic framework materials are often capable of reproducing the architectures of well-known inorganic materials, and there is therefore substantial interest in metal-organic perovskite analogues and their functional properties. In particular, much recent work has focused on the family of formate perovskites, in which the formate anion HCO_2^- replaces oxide or fluoride on the X linker site.[4–7] The use of a polyatomic linker increases the cell volume such that the A site can itself be occupied by a larger, polyatomic cation, yielding a series of perovskite analogues of general formula $A[M(HCO_2)_3]$. Known A site cations include dimethylammonium (DMA),[5] ammonium,[8] guanidinium,[9] and imidazolium;[10] occupying the M sites in these materials are divalent metal ions Mg, Mn, Fe, Co, Ni, Cu, or Zn.

Members of the specific family of materials with A = dimethylammonium[11] are known to have several of the important properties of the inorganic perovskites, including multiferroicity[12] with magnetoelectric[13] and magnetoelastic[14] coupling. These materials crystallise in space group $R\bar{3}c$ at room temperature, with the dimethylammonium ions ordering ferroelectrically at lower temperatures, causing a first-order phase transition to space group Cc (Fig. 1).[5] This ordering arises from hydrogen bonding between the nitrogen atoms of the guest DMA cations and the oxygen atoms of the formate framework;[15] however, these interactions are subtle and not yet fully understood. For instance, the M = Co system displays the two phases described above when prepared without isotopic substitution, yet the perdeuterated material shows an additional phase transition above room temperature.[16] However, it is precisely these hydrogen bonding interactions that must be understood if crystal engineering of new metal-formate perovskites with targeted properties is to be successful.

In addition to crystallographic methods, the nature of the phase transition has been explored by dielectric measurements and calorimetry.[5,7] These, however, are all bulk probes; in particular standard diffraction analysis reveals only the crystal structure averaged over all unit cells in the sample, potentially giving an incomplete or even seriously misleading picture of the local

---

[a] School of Physics and Astronomy and Materials Research Institute, Queen Mary University of London, London E1 4NS, U.K. E-mail: a.e.phillips@qmul.ac.uk

[b] ISIS Neutron and Muon Source, Rutherford Appleton Laboratory, Harwell Oxford, Didcot OX11 0QX, U.K.

† Electronic Supplementary Information (ESI) available: raw data, full details of restraints applied during refinement, tables of lattice parameters, details of convergence criteria, and details of representative initial and final configurations. See DOI: 10.1039/b000000x/

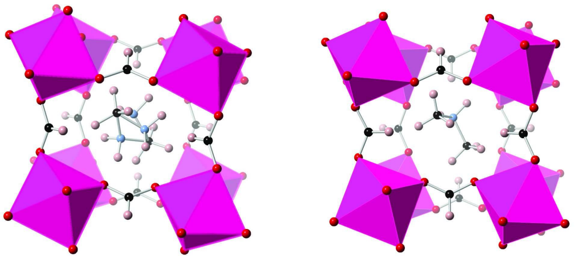

Fig. 1 $(CD_3ND_2CD_3)Mn(DCOO)_3$ in the high (left) and low (right) temperature phases, shown as the pseudocubic unit cell. The Mn^{2+} are linked by the formate framework to form MnO_6 octahedra (bright pink). The DMA cation in the cage (with blue nitrogen, black carbon and pale pink hydrogen) is disordered in the high temperature phase, with partial occupancy of three sites for the ND_2 groups.

interactions involved in the hydrogen bonding. For this reason methods sensitive to local interactions, such as vibrational spectroscopy[15,17] and NMR[18,19] are also important to characterise these systems.

We focus here on a different local probe: total neutron scattering, which gives direct information about local deviations from the spatial average structure determined by standard crystallographic methods. Neutron scattering is particularly suitable for these experiments firstly because it is sensitive to the positions of hydrogen atoms, which are vital to understand hydrogen bonding. Second, as data can be measured to high scattering vectors, high-resolution pair distribution functions are determined.[20] In this paper we report data from perdeuterated dimethylammonium manganese formate powder (T_c = 183 K) in the high- and low-temperature phases. Analysing the total neutron scattering from this material, using the reverse Monte Carlo (RMC) method to produce atomic models consistent with all experimental data, allows us to model the hydrogen-bonded interaction between the dimethylammonium cation and the framework. From this in turn we infer details of the dynamics of the cation in the pores of the framework and the role of the framework itself in mediating guest-guest interactions across the phase transition.

2 Methods

2.1 Synthesis

The sample was synthesised by literature methods:[11] 1.42 g $MnCl_2 \cdot H_2O$ was dissolved in 10.69 g D_2O and a 10 g ampoule of $CDON(CD_3)_2$ added. The resulting mixture was heated in a sealed pressure vessel to 140 °C for three days and then cooled to room temperature. On opening the vessel pale pink crystals of DMMnF had already formed; these were filtered, washed with CD_3OD and dried under suction, giving a yield of 1.67 g (70%). The ^1H from the water of crystallisation of the manganese(II) chloride was calculated to be at most 1% of the total hydrogen content of the system, and proved to be undetectable in subsequent neutron analysis.

2.2 Data collection

Neutron scattering data were collected using the `GEM` diffractometer at the ISIS facility, UK. The entire sample was loaded into an 8 mm vanadium can. Total scattering measurements, with a minimum collection time of eight hours, were carried out at several temperatures between room temperature and 7 K.

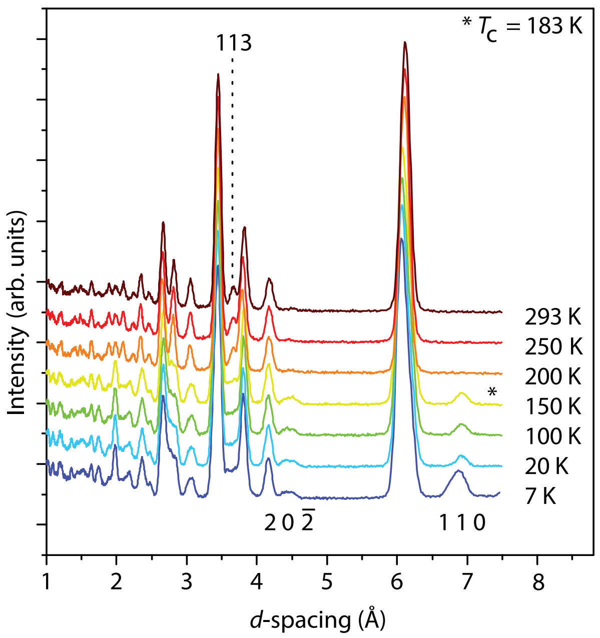

Fig. 2 Observed diffractograms for DMMnF in the $R\bar{3}c$ ($T > 183$ K) disordered phase and in the Cc ($T < 183$ K) ordered phase.

Room temperature measurements were taken in the diffractometer with no additional sample environment; all measurements below room temperature were taken in a closed cycle refrigerator. Additionally, for normalisation and background subtraction purposes, data were collected from the empty instrument, the empty refrigerator, a solid vanadium rod, and an empty can identical to the sample container in the refrigerator. As well as the total scattering collections, shorter runs suitable for standard diffraction analysis with one hour collection times were taken at 10 K intervals between 200 K and 150 K, across the phase transition. Details of the collection run numbers can be found in the ESI.†

2.3 Rietveld analysis

The diffraction data were analysed by the Rietveld method,[21] carried out using `GSAS`[22] and the `EXPGUI` interface.[23] Starting configurations were obtained from literature X-ray structure determinations.[7] `GEM` detector banks 2–5 were refined simultaneously; the background was modelled as a ten-term shifted Chebyshev polynomial while the peak profiles were fit using GSAS' type 2 time-of-flight profile function, which combines a pseudo-Voigt peak shape with the Ikeda-Carpenter moderator pulse shape. Least-squares refinement was carried out by varying the parameters in the following order: cell parameters, peak-shape parameters, DMA deuterium coordinates, deuterium isotropic displacement parameters, and all atomic coordinates and isotropic displacement parameters. The `DIFA` coefficient, representing quadratic dependence of time of flight with respect to d-spacing, was also refined in order to compensate for absorption in the sample. Bond length restraints were applied to intramolecular covalent bonds (see ESI for full details),† and constraints were used to ensure the isotropic atomic displacement parameters of all atoms of the same type were consistent.

The observed diffractograms from bank 2 ($13° \leq 2\theta \leq 21°$), which was used in subsequent RMC refinement, are given in

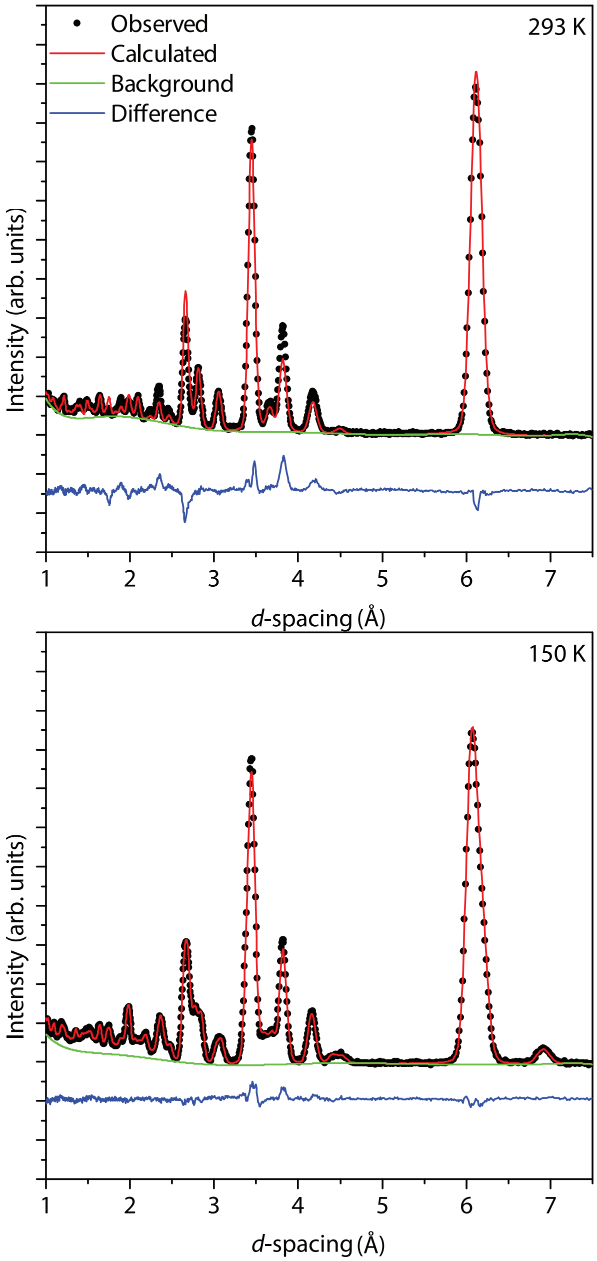

Fig. 3 Rietveld refined Bragg profiles for DMMnF in the paraelectric phase (top, 293 K) and the antiferroelectric phase (bottom, 150 K). The poorer fit of the HTP to the data than the LTP is due to the simplified model of disorder used; see main text.

figure 2. The phase transition to the electrically ordered phase is clearly visible from the new peaks with *d*-spacing of 6.90 Å (110) and 4.39 Å ($20\bar{2}$) (where the Miller indices are given with respect to the low-temperature cell). Similarly, the high-temperature (113) reflection at 3.66 Å is lost as a sharp peak, although a feature with substantial intensity remains in this region of the diffraction profile. Representative refinements for both phases are given in figure 3. The poorer fit of the high temperature phase is a result of the $R\bar{3}c$ model, which for simplicity had an ordered arrangement of the methyl groups, with the local threefold axis aligning with the crystallographic threefold axis, so that the only disordered moiety was the ND_2^+ group but the D–C–N angles were unrealistic. A more realistic model of the dynamic disorder would take into account the reorientations of the methyl groups as well, as was done in the RMC refinement, indeed producing a better fit.

2.4 Pair distribution functions

Using `GUDRUN`, the scattering function $F(Q)$ was extracted from the data, and corrections for sample environment, beam attenuation, absorption, and inelastic scattering were applied (see ESI).† The Q range 0.7 Å^{-1} to 42 Å^{-1} was transformed to give the pair distribution function $D(r)$ according to

$$D(r) = \frac{2}{\pi}\int QF(Q)\sin(Qr)\,\mathrm{d}Q. \qquad (1)$$

2.5 Reverse Monte Carlo modelling

Atomistic models consistent with the scattering data were generated using the reverse Monte Carlo (RMC) method, in which random atomic displacements are applied to a starting configuration according to the Metropolis algorithm, as implemented in `RMCProfile` version 6.5.[24] This software calculates the pair distribution function $D(r)$, the scattering function $F(Q)$, and the Bragg intensities $I(hk\ell)$ from a model configuration of atoms, typically approximately a cube of side length 50 Å. The first two functions are directly compared with experimental data while the Bragg intensities are combined with peak shape and background functions taken from Rietveld analysis in order to compare the model with the experimental Bragg profile.

Starting configurations were generated from supercells of the refined crystal structures: the high-temperature $6 \times 6 \times 2$ supercell, containing 10 368 atoms, had a volume of around 99 000 Å^3, while the low-temperature $4 \times 6 \times 6$ supercell contained 13 824 atoms with a volume of around 130 000 Å^3. To generate starting configurations for the high-temperature phase, a model of the disorder in the average crystal structure was required. We tested three different starting configurations that differed in the orientations of the DMA ions about the threeforld axis. In the first, the angles of rotation of the ND_2 groups were uniformly distributed across a full revolution; in the second, they were distributed equally among the three values at each site suggested by the average crystal structure; and in the third, refinement started from a single one of these angles. No disorder was introduced into the initial orientation of the DMA cation in the starting configurations of the electrically ordered phase: attempts to refine a disordered model against data from the ordered phase converged at substantially higher χ^2 values, so that the resulting models were not considered plausible.

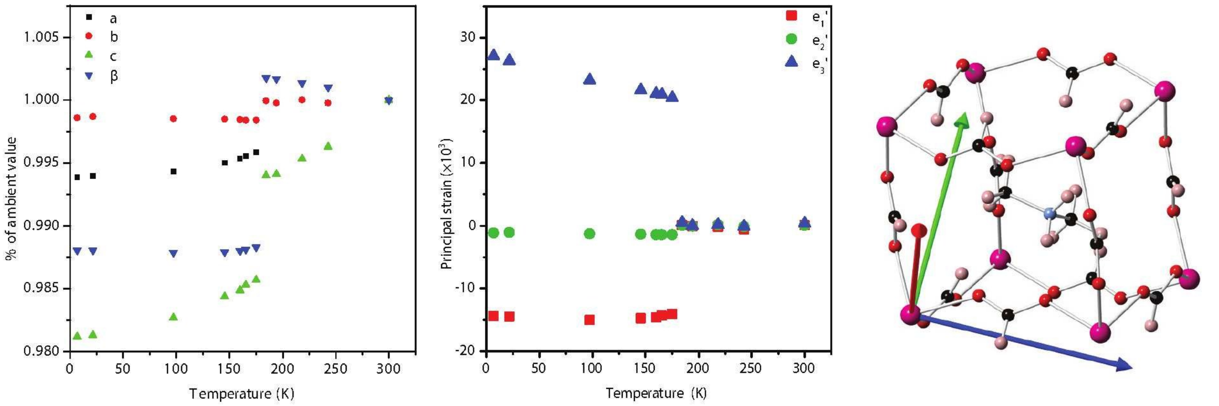

Fig. 4 Left: the lattice parameters of DMMnF across the phase transition, expressed in terms of the monoclinic *Cc* setting, relative to the $T = 293$ K values. Centre: principal strain components e_1' (red), e_2' (green) and e_3' (blue) as a function of temperature. Right: the corresponding eigenvectors.

The χ^2 value for each trial configuration was the weighted sum of the values calculated from the pair distribution function $D(r)$, the scattering function $F(Q)$, the diffraction intensity $I(t)$, and three artificial partial pair distribution functions (see below) in $1:2:1:0.02$ ratio, plus a restraint term. This final term was used to apply Morse stretch and harmonic cosine bending potentials to the molecules in the system: these and distance windows preventing bound atomic pairs from moving too far apart were necessary to prevent the DMA and formate molecules from refining to chemically unreasonable positions. The energy prefactors D for the bond stretching and k for the bending potentials, and the equilibrium angles θ_0 for the bond bending angles, are taken from the standard MM3 potentials, while the equilibrium bond lengths r_0 for the stretching potentials were chosen for consistency with the experimental pair distribution functions. Full details of these potentials are given as ESI.†

Very weak artificial partial pair distribution functions $g_{\mathrm{CD}}(r)$, $g_{\mathrm{ND}}(r)$, and $g_{\mathrm{CO}}(r)$ were included for $r \leq 1.5$ Å in order to prevent the stretch potentials from producing unphysically bimodal distributions for the overlapping bond lengths in this region. To ensure that these conditions did not bias the conclusions of this study, control refinements were performed in each phase including all restraints and other external information but without incorporating any experimental data.

Refinement was continued until the χ^2 values did not improve significantly with further iterations (see ESI); typically this took 1.5×10^7 atomic moves.† Statistics were collected for analysis by combining 30 configurations at each temperature.

3 Results

3.1 Strain analysis

Before the detailed reverse Monte Carlo analysis, we consider the experimentally refined lattice parameters as a guide to the phase transition. In order to compare the two phases directly, the high temperature phase $R\bar{3}c$ lattice parameters ($\mathbf{a}_h$, $\mathbf{b}_h$, $\mathbf{c}_h$) were expressed in terms of the monoclinic *Cc* low temperature phase ($\mathbf{a}_m$, $\mathbf{b}_m$, $\mathbf{c}_m$) according to reference 7:

$$\mathbf{a}_m = -\mathbf{a}_h - 2\mathbf{b}_h \tag{2a}$$

$$\mathbf{b}_m = -\mathbf{a}_h \tag{2b}$$

$$\mathbf{c}_m = \tfrac{1}{3}\mathbf{a}_h + \tfrac{2}{3}\mathbf{b}_h - \tfrac{1}{3}\mathbf{c}_h \tag{2c}$$

Figure 4 shows the change in the lattice parameters as a function of temperature as the material cools below T_c. A sharp discontinuity in all lattice parameters is seen between 180 K and 190 K, consistent with a first-order phase transition, and confirming that the temperature of the transition of the deuterated analogue is consistent with that of the previously reported transition on the ^{1}H-containing material.[12,17] A table of the refined lattice parameters can be found in the ESI.†

The lattice parameters of the high temperature phase were extrapolated linearly to 0 K and used to calculate the linear Eulerian strain tensor e_{ij}.[25] The principal components e_1', e_2' and e_3' were calculated by diagonalising this tensor (Fig. 4). According to Landau theory these strains will be proprtional to the square of an order parameter η^2, which is a measure of the degree of orientational order of the DMA cations. The component e_3' continues to increase on cooling below T_c, suggesting that the DMA cations continue to order even below the phase transition, consistent with results from vibrational spectroscopy.[17] If it is assumed that the DMA cations are fully ordered at 7 K, then this analysis implies that at 180 K, although still below the phase transition temperature, approximately 13% of the disorder found in the high-temperature phase is already present.

The principal axis of the strain tensor corresponding to the most positive strain (e_3') is about 20° away from the DMA C···C axis, close to the pseudocubic [111] direction; the axis corresponding to the most negative strain (e_1') is about 20° away from the normal to this axis (Fig. 4). These results already suggest that the phase transition corresponds to a contraction of the framework about the guest cation, corroborating both previous work and our subsequent RMC analysis below.

3.2 Pair distribution functions

The short-range region of the experimental pair distribution functions are shown in figure 5. As expected, below 4 Å, the observed peaks correspond to intramolecular bonds, and hence the low and high temperature data are very similar. However, at $r > 7.5$ Å, the peaks of the high and low temperature phases become distinct, with strong peaks at 8.44 Å and 9.00 Å emerging in the low-temperature data. That the phase transition is so clearly detectable in the pair distribution functions is characteristic of first-order behaviour.

Using the Faber-Ziman formalism,[26] the pair distribution func-

This journal is © The Royal Society of Chemistry [year]

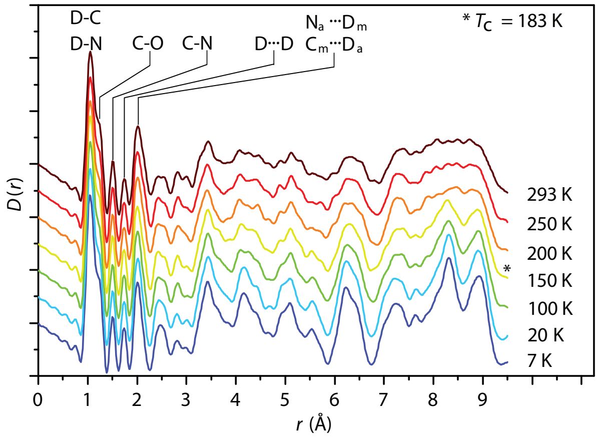

Fig. 5 The pair distribution function $D(r)$, $r \leq 9.5$ Å derived from total scattering experiments, with low-r peaks identified.

tion $D(r)$ can be understood as a sum of partial PDFs $g_{ij}(r)$ corresponding to specific pairs of atom types. The contribution of each partial PDF to the total is weighted by the fraction of atoms of the relevant types c_ic_j, by the coherent bound scattering lengths of the relevant species b_ib_j, and by a factor of 2 for heteroatomic pairs to account for the fact that the functions $g_{ij}(r)$ and $_{ji}(r)$ are identical. These products are given in Table 1 in descending order of absolute value. The greatest contributions, due mostly to the large amounts of the relevant elements present in this material, are from the D···D, D···O, and D···C pairs, which between them account for 64% of the scattering.

To assess the extent to which the average crystal structure provides an accurate model of this material's local structure, this formalism was used to generate pair distribution functions from the average crystal structure. In the high-temperature phase, each dimethylammonium nitrogen atom was randomly assigned to one of the three split sites related by the threefold axis, and deuterium atoms were then located in ideal positions (bond lengths and angles taken from the MM2 potentials set and methyl groups staggered with respect to the ammonium group). To assist visual comparison with the experimental data, the pair distribution functions were then convolved with a Gaussian of standard deviation 0.1 Å in the high-temperature phase and 0.05 Å in the low-temperature phase.

The resulting pair distribution functions and their experimental counterparts are shown in figure 6. Considering the peaks in order, in the high-temperature phase, those corresponding to the D–C and D–N bonds at 1.06 Å and C=O bonds at 1.24 Å match well. The C–N peak at 1.51 Å, however, is noticeably longer than suggested by the split-site model (1.42 Å). This shows that the distance of the nitrogen atom from the threefold axis is underestimated in the average crystal structure, as expected in cases where substantial rotational freedom is modelled by a single displacement ellipsoid. There is then reasonable agreement in the positions of the following peaks at 1.74 Å and 2.01 Å, which account respectively for D···D distances across a single methyl or ammonium group and for O···DC, C···DN, and N···DC distances internal to the formate and dimethylammonium ions. The 2.01 Å peak also includes the first intermolecular correlation, corresponding to a hydrogen-bonded D···O distance between dimethylammonium and formate ions.

The region immediately above 2 Å, by contrast, displays a

Table 1 Faber-Ziman weighting factors $(1+\delta_{ij})b_ib_jc_ic_j$ for the partial pair distribution functions' contribution to the total PDF

Atom pair i,j	$b_ib_jc_ic_j$ (fm^2)
D, D	9.349
D, O	8.871
D, C	8.567
C, O	4.017
D, N	2.385
O, O	2.105
C, C	1.917
O, N	1.132
C, N	1.080
D, Mn	–0.950
O, Mn	–0.451
C, Mn	–0.430
N, N	0.152
Mn, N	–0.121
Mn, Mn	0.024

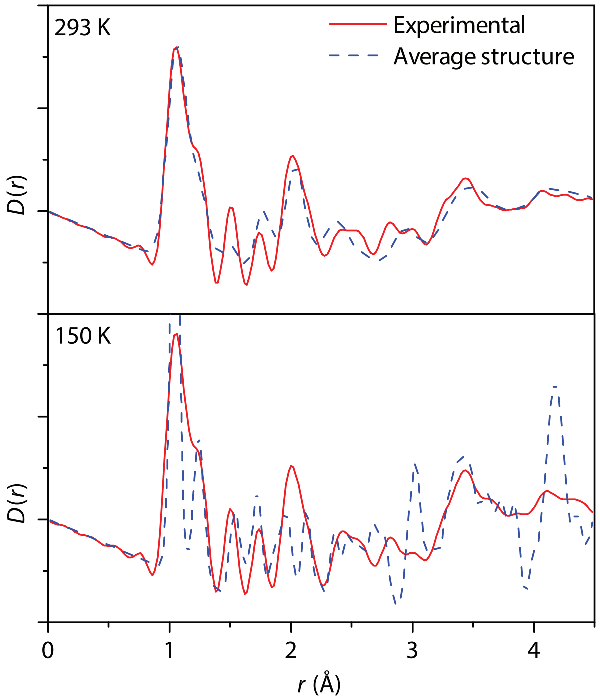

Fig. 6 The experimental pair distribution functions in both phases show broad agreement at low r with those expected from the average crystal structures, but deviate above around 2 Å. The calculated PDFs were broadened by convolution with a Gaussian of standard deviation 0.1 Å (293 K data) or 0.05 Å (150 K data).

marked disagreement between the average and experimental PDFs. As the number of theoretically distinct PDF peaks increases rapidly with increasing r, we list here only peaks up to 2.8 Å. The weak, negative Mn–O peak at 2.19 Å is apparent in the average structure but not resolvable in the experimental PDF. This region of the PDF still includes intramolecular peaks, including the formate O···O at 2.22 Å and dimethylammonium D···D at 2.27 Å, 2.32 Å, 2.64 Å, and 2.90 Å; C···C at 2.47 Å; and C···DC at 2.76 Å. However, it also includes intermolecular peaks between the dimethylammonium and formate ions, related to the position of the guest ions within the framework. These include ND···D and ND···C at 2.43 Å; ND···O at 2.47 Å; CD···C at 2.54 Å; CD···O at 2.66 Å and 2.82 Å; and CD···D at 2.71 Å and 2.85 Å (where in each case the dimethylammonium atom is listed first).

In the low-temperature phase, the situation is similar in that the intramolecular peaks up to $r = 2$ Å match well, with noticably better agreement in the position of the C–N peak at 1.52 Å, whereas there are substantially greater discrepancies at 2 Å and above.

3.3 Reverse Monte Carlo modelling

The functions $D(r)$, $I(t)$, and $F(Q)$ calculated from converged RMC models showed good agreement with the data (Fig. 7). A detailed analysis of the geometry of the converged models was therefore performed. We ascribe the improvement of the $I(t)$ with respect to the Rietveld refinement to the more realistic CD_3 geometry in this model.

3.3.1 Orientational distribution of the dimethylammonium cations

In the high-temperature phase, the refined distribution of angles of the DMA cations was found to depend on the starting configuration. Starting from a uniform distribution of angles (model **1**), six maxima evolved (Fig. 8a). As expected, these include large maxima at the angles corresponding to the disordered model of the average crystal structure, corresponding to hydrogen bonds between the ND_2^+ group and two adjacent formate ions (Fig. 9a). However, smaller maxima between these angles were also formed. These positions correspond to hydrogen bonds between the ND_2^+ group and two oxygen atoms belonging to the same formate, which is also a chemically plausible hydrogen-bonding geometry (Fig. 9b).

On the other hand, starting from the three angles at each site suggested by the average crystal structure (model **2**) gave a refined distribution of angles in which the three maxima broadened but no new peaks were formed (Fig. 8b). Starting from a single angle at each site (model **3**) similarly failed to reproduce even the other two major maxima (Fig. 8c).

These results suggest that the experimental data are comparatively insensitive to the distribution of these angles, with several local minima in configuration space of comparable goodness of fit: if these configurations had substantially different χ^2 values, the Metropolis algorithm should prevent the refinement from converging to the worse fitting model. Indeed, the χ^2 values calculated for the three starting configurations were very similar for the three experimental data sets and in total (Fig. 10). Comparing model **1**, with additional orientations of the DMA cation, with model **2**, suggested by the average crystal structure, shows that model **1** is slightly favoured by the real-space data

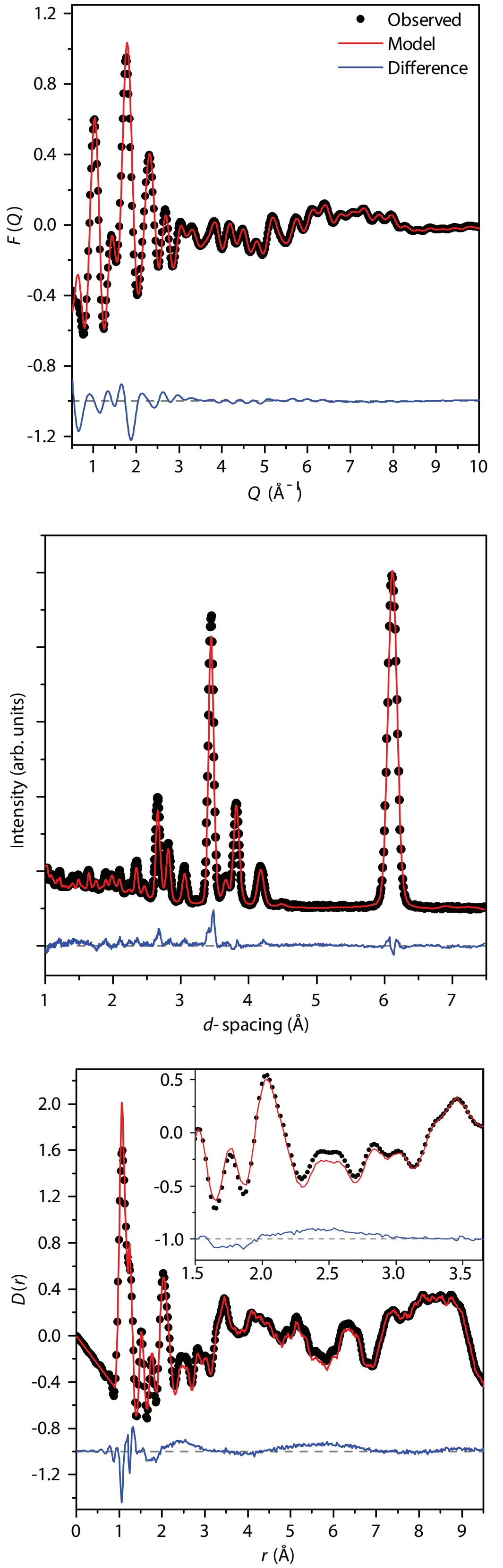

Fig. 7 The $D(r)$, $I(t)$, and $F(Q)$ functions observed experimentally and calculated from a converged configuration at room temperature. Observed values in black; calculated values in red; difference in blue.

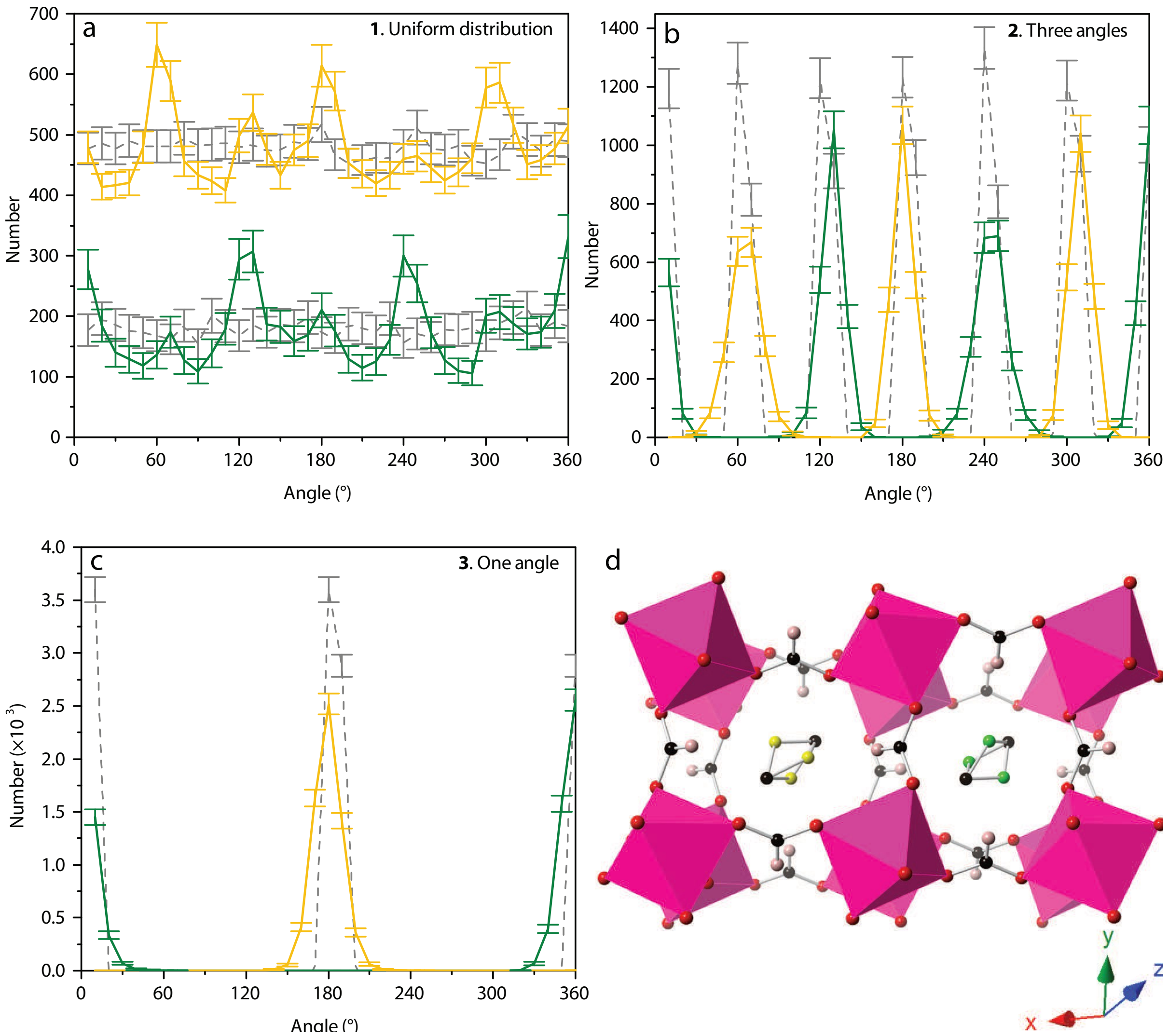

Fig. 8 The angle of DMA rotation, defined as the angle between the vector from the centroid of the molecule to the nitrogen atom and the crystallographic a axis, for the initial (grey) and final (colour) configurations of the $293\,\mathrm{K}$ data for refinements (a) starting from a uniform distribution of angles (**1**); (b) starting from three angles at each site, as suggested by the average crystal structure (**2**); and (c) starting from a single angle at each site (**3**). The two sites related by the c glide plane (d) are distinguished by yellow and green lines, which in (a) have been offset by 400 for clarity.

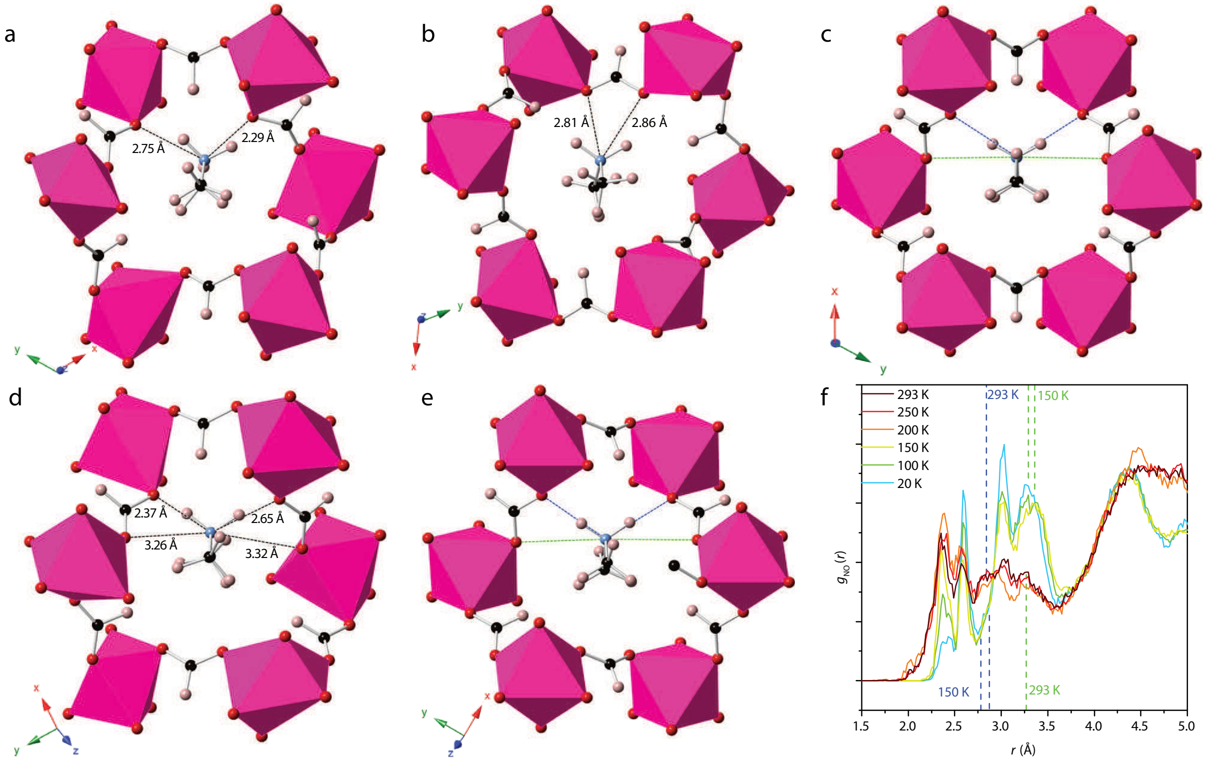

Fig. 9 (a) A representative final configuration from the high-temperature phase, showing the DMA ion bound to two adjacent formate ions in a major maximum of the angle distribution (see Fig. 8). The N···O distance is substantially shorter than in the average crystal structure (see c) but the topology is identical, with the ammonium moiety caught in a Mn(DCO_2)$_2$ "pincer". (b) A representative final configuration from the high-temperature phase, showing the DMA ion bound to the two oxygen atoms of a single formate ion in a minor maximum of the angle distribution (see Fig. 8). (c) The average crystal structure of the high-temperature phase. (d) A representative final configuration from the low-temperature phase. (e) The average crystal structure of the low-temperature phase. (f) The partial pair distribution function $g_{\mathrm{NO}}(r)$ from RMC refinement shown at all temperatures across both phases. Dashed lines indicate the N···O separations from the average crystal structures of both phases. All data in this figure come from starting configurations with a uniform distribution of DMA orientations (model **1**).

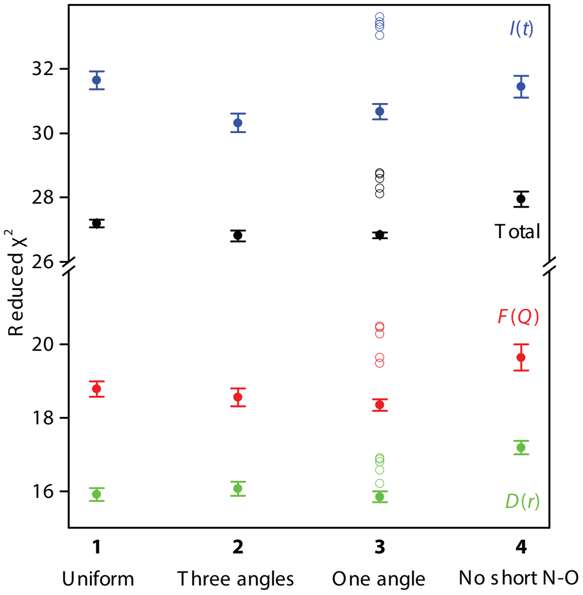

Fig. 10 Refined chi-squared values for models with varying restraints and starting configurations. The error bars shown are the standard deviations of thirty refinements, except in the case of model **3**, where five refinements converged to substantially different chi-squared values and are plotted separately.

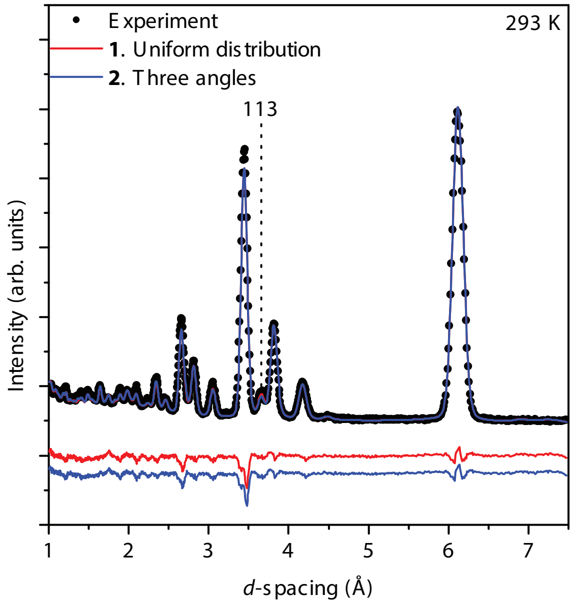

Fig. 11 The difference between the quality of the fits of models **1** and **2** to the Bragg diffraction data is not readily visible. The most obvious difference in intensity is in the (113) peak, which is expected since this peak is sensitive to the distribution of the DMA orientation angles, disappearing altogether at the ordering transition.

while model **2** is slightly favoured by the reciprocal-space data. However, these differences are minimal: for both the PDF $D(r)$ and scattering function $F(Q)$ the range of χ^2 values obtained from thirty refinements overlapped. For the Bragg profile $I(t)$, the range of χ^2 values for the two models did not overlap, but the difference was nonetheless relatively small, with very little visible change in the quality of the fit (Fig. 11).

For model **3**, five of the thirty refinements converged to substantially higher χ^2 values than the remaining 25, and are for this reason plotted separately in Fig. 10. Other than the χ^2 values, little clear difference, either in the atomic configurations or in the fits to the experimental data, was observed between these and the remaining 25 refinements to this model. It is perhaps not surprising, given that this starting configuration is deliberately far from the average structural model, that a variety of local minima were found in this case, and this wide distribution of final χ^2 values is an indication that these refinements should be treated with caution. However, the fact that the χ^2 values are comparable to (and even, if the five outliers are excluded, lower than) those from the more realistic models is a further indication of the limited sensitivity of the data to the distribution of DMA orientations.

Although there is some difference between reported measurements, most previous work has suggested that the entropy change across the phase transition is $\Delta S/R \approx \ln(3)$, consistent with the freezing of threefold disorder.[7] In order to compare our own distributions to this value, we estimated the entropy of each phase due to cation rotation using the relationship from statistical mechanics

$$S_{\text{molar}} = -R\sum_i p_i \ln p_i \qquad (3)$$

where the sum is over microstates i with respective probabilities p_i. In our analysis we divided the histogram of rotation angles (Fig. 8) into bins of equal size and assumed each bin to be a single "microstate". For model **1**, this suggested a higher entropy change of $\Delta S/R \approx \ln(6.4)$. The major reason for the discrepancy between this simple calculation and the experimental result is likely to be that estimating the entropy based on the orientation angle alone, in the same manner as the ln(3) estimate from the average crystal structure, does not take into account correlations between the motion of the cation and the framework. These will reduce the entropy of the high-temperature phase and hence the entropy change associated with the phase transition. The discrepancy suggests, therefore, that such correlations are important in this system, as we shall further see below.

Using the same method of estimating the rotational entropy change across the phase transition for model **2**, based on the average crystal structure, gave a value of only $\Delta S/R = \ln(2.1)$. This suggests that, when the distribution of angles is taken into account, in this model the rotational entropy is not sufficient to account for the experimentally observed entropy change, which would have to come from changes in the framework. The equivalent result for model **3** was negative, $\Delta S/R = -\ln(1.2)$.

To summarise this part of the analysis: it is striking that the RMC refinements (**1**) starting from uniform distributions of the DMA cations consistently converged to a new, chemically plausible distribution with smaller probability maxima between the known threefold disorder. Moreover, within the limits of a rough entropy calculation this analysis is consistent with the host-guest hydrogen bonding causing correlations between the cation orientation and framework motion. However, the very small differences in χ^2 values between models starting from different configurations, the visual similarities between the fits, and the fact that the refined distribution is so strongly dependent on the starting configuration all emphasise the subtlety of the effects of cation orientation on the experimental data. Our observations are also consistent with the trimodal distribution suggested by the average crystal structure, and further work will be necessary to distinguish between these two models.

3.3.2 Hydrogen bonding and nitrogen-oxygen distances

Further information about the hydrogen bonding comes from the observed N···O distances. We first describe here the situation in refinements starting from a uniform distribution of DMA angles (model **1**; Fig. 9) before considering how this varies depending on the starting configuration. In both phases, peaks are observed in the partial pair distribution function $g_{\mathrm{NO}}(r)$ at approximately 2.4 Å and 2.6 Å. These differ from the average crystal structure in two important ways: first, the two shortest N···O distances are not the same length; second, they are substantially shorter than the distances inferred from the average structure. The first point is not especially unusual: there are many examples, for instance, in the Cambridge Structural Database of compounds with multiple hydrogen bonds differing by 0.2 Å, even between chemically similar or identical pairs. The second point is more unexpected, since only a handful of examples are known in which the average crystal structure has N···O separations as short as this. We suggest, however, that these reflect short-lived separations resulting from the distortion of the ideal framework to accomodate the particular instantaneous orientation of the guest cation. The fact that the peak positions remain constant across the phase transition indicates that these indeed show favourable local geometries rather than longer-range interactions.

On cooling in the low-temperature phase, the 2.4 Å peak decreases in intensity while the 2.6 Å peak increases. This suggests that maintaining very short bonds involves an unacceptable distortion of the framework at very low temperatures, so that at 20 K almost all N···O nearest neighbours are around 2.6 Å apart. This is nonetheless substantially shorter than seen in the average structure (Fig. 9), implying that it involves a local distortion about particular cations. This change in peak intensity on cooling the low-temperature phase suggests a mechanism for the ordering inferred from the strain analysis above.

The N···O pair density is also more structured in the range 3.0 Å to 3.5 Å in the low- than in the high-temperature phase, suggesting that more distant formate ions also freeze into longer hydrogen bonds as the framework contracts about the guest cation during the phase transition.

It is important here to note that, although the partial pair distribution function $g_{\mathrm{N,O}}(r)$ is a convenient way to visualise the distribution of the hydrogen bonding in this material, it is not itself a major contributor to the total pair distribution function $D(r)$ because of its relatively small weighting factor (Table 1). However, because the parameters of the RMC fitting process are the individual atomic positions rather than the partial pair distribution functions themselves, this fit is coupled to the intramolecular potentials applied and to the other partial pair distribution functions. In particular, the N···O distances are strongly related to the highly weighted D···O distances via the ammonium D atoms.

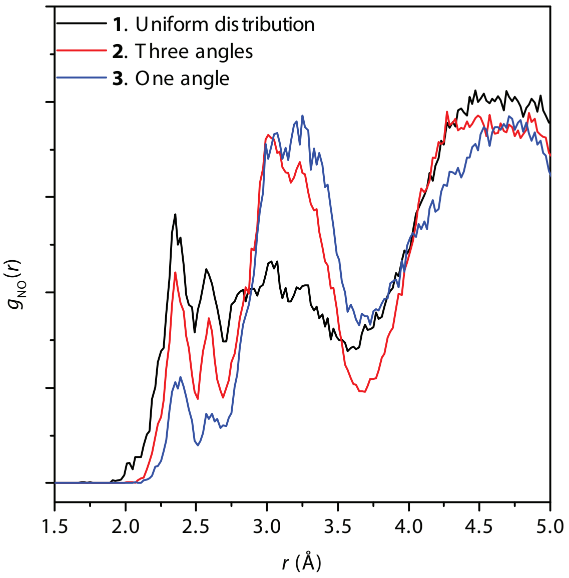

Fig. 12 Partial pair distribution functions $g_{\mathrm{N,O}}(r)$ from models starting from different distributions of the DMA cations. Although the relative magnitude of the peaks differs, their location remains the same.

Given the differences in DMA orientation observed depending on the starting configuration for refinements of the high-temperature data, we calculated the N···O partial pair distribution function for all three starting configurations (Fig. 12). Although the peaks are in the same places for the three starting configurations, their relative sizes differ, with fewer dimethylammonium ions hydrogen-bonded to the framework in the second and third cases and more moving well away from the formate ions. Nonetheless, the fact that these shorter hydrogen bonds are found regardless of the initial configuration is an encouraging indication of the robustness of this result.

To confirm this, we finally performed a fourth set of refinements on the high-temperature phase in which no move was accepted that would bring an N···O distance closer than 2.8 Å, well within the 2.93 Å suggested by the average crystal structure. This model **4** gave a substantially poorer fit to all three experimental data sets (Fig. 10).

The dependence of the N–D stretching frequencies on temperature and deuteration has previously been measured by Raman and IR spectroscopy and interpreted on the basis of the average crystal structure model.[17] Several peaks were assigned to N–D stretching, rather than the clear pair of symmetric and antisymmetric stretch that might be expected from two equal hydrogen bonds; thus the reported peak assignments appear consistent with our model.

On the basis of the frequencies compared to those of N–D groups not involved in hydrogen bonding and the size of the Ubbelohde effect (the increase of the hydrogen bond length on deuteration), the hydrogen bonding was determined to be of medium strength. This strength is consistent with our observed N···O peak at 2.6 Å. On the other hand, an equilibrium N···O distance of 2.4 Å, which is also suggested by our model, would be typical of strong hydrogen bonding.[27] At this distance, there should be little barrier to hydrogen transfer between the formate

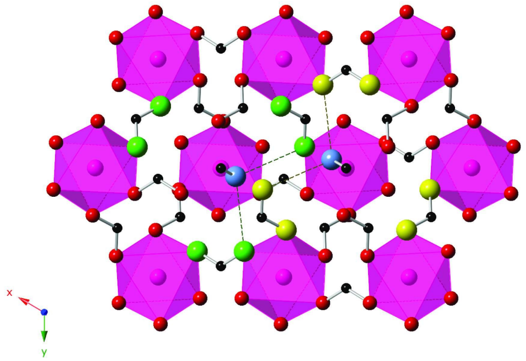

Fig. 13 Section of the framework showing two adjacent pseudocubic cages. For clarity, oxygen and nitrogen atoms are enlarged and hydrogen is not shown. The six oxygen atoms to which the DMA cation on the left can hydrogen bond are shown in green, the six to which the cation on the right can hydrogen bond in yellow.

and ammonium ions.[28] While such a transfer, moving towards dimethylamine and formic acid, is chemically plausible, it is known on the basis of dielectric measurements not to be the major effect responsible for the phase transition.[17] Moreover, it was explicitly not taken into account in the present study, in which intramolecular potentials were applied to the ammonium N–D bonds.

However, rather than a true equilibrium position, this shortest distance may instead be best interpreted as an instantaneous snapshot of the rotation of the DMA cation. Indeed, the vibrational study revealed a pronounced sharpening of the N–D stretching mode on cooling through the phase transition, indicating that the hydrogen bonding in the high-temperature phase is both dynamic and anharmonic.[17] This interpretation of the 2.4 Å peak is also supported by our observation that it decreases in intensity on cooling in the low temperature phase, as the DMA motion freezes out. Our observations of continued ordering on cooling below the phase transition, from both the cell parameters and the N···O distances, are again consistent with the vibrational study, which showed that the intensity and frequency of the N–D stretching peaks increase, and the FWHM decreases, on cooling, signatures of continued ordering.

To investigate the interaction between neighbouring electric dipoles, the angle between the dipole moment of each DMA cation and each of its six nearest neighbours was calculated for the high and low temperature phase models. However, in the high-temperature phase, no deviation from the random initial orientations could be detected. Similarly, in the low-temperature phase, the refined distribution of dipole-dipole angles was consistent with the average crystal structure. It is not surprising phenomenologically that no correlations between neighbouring dipoles were observed above the transition temperature, since for a first-order phase transition the correlation length will be small even immediately above the phase transition. Although from a microscopic perspective, given the strong framework-cation interactions, stronger correlations mediated by the framework might have been expected, the formate ions potentially involved in hydrogen bonding, at either major or minor maxima, are distinct for nearest-neighbour DMA ions (Fig. 13). Thus the framework-cation interactions, although strong, are relatively independent of one another; the driving force for the phase transition is the collapse of the framework rather than the electric ordering that emerges as a consequence.

Having seen that the framework buckles about the guest cation, we finally investigated the distortion of the MnO_6 octahedra. In the high temperature phase, the distribution of the angles remains largely unchanged, including the bimodal character at around 90°, while in the low temperature phases, there is significant broadening.† Despite the differences between the geometry of the two phases, however, the r.m.s. distance of the Mn ions from the centroid of the O_6 octahedra remained roughly constant at 1.2 Å across both phases. This suggests that distortion of the coordination octahedra does not play a substantial role in the phase transition.

4 Conclusions

Reverse Monte Carlo modelling suggests the presence, in both phases of this material, of shorter hydrogen bonds than are apparent from the average crystal structure. The shortest of these, at around 2.4 Å, appear transient and are less accessible at low temperatures, while those at around 2.6 Å remain at all temperatures studied. In the low-temperature phase there is some additional structure in the N···O partial pair distribution function at higher r, suggesting the formation of weaker hydrogen bonds with other formate ions in the framework.

The principal components of the strain tensor for the low temperature phase also show that the framework contracts about the DMA ion during the phase transition. They further suggest that the ordering process continues below T_c, corroborating the RMC hydrogen-bonding model.

The threefold disorder of the DMA ND_2 observed in the high-temperature crystal structure is reproduced in the RMC models only for nearby starting configurations. For a uniform starting distribution, these models also show the presence of smaller minima between these three positions. The resulting entropy change is estimated to be higher than the experimental value, suggesting that correlations between the cation and framework in the high-temperature phase are important and reduce the entropy of this phase below that expected from the cation alone. The dependence of these results on the starting configuration, and the low χ^2 values obtained for the deliberately incorrect model containing a single starting orientation, suggest that the experimental data reported here are relatively insensitive to the orientational disorder of the DMA ion. Further work will be necessary to demonstrate the unambiguous existence of these new hydrogen-bonded geometries.

Little evidence of dipole interactions between nearest-neighbour DMA cations in the either phase was observed. This appears to be due partly to the first-order nature of the phase transition and partly to the specific geometry of the guest-framework interactions, which allow nearest neighbours to rotate almost independently even when the response of the framework is taken into account.

More generally, total neutron scattering is a promising technique for investigating the phase transition in materials similar to this, producing data that are sensitive to both local and long-range order. In systems where these data are also sensitive to the ordering process, therefore, we anticipate that it will be an important tool for studying the atomic origins of desirable electric properties in metal-organic frameworks.

Acknowledgements

We thank the EPSRC for provision of the MidPlus high-performance computing system on which the calculations were performed (EP/K000233/1, EP/K000128/1) and for support to AEP (EP/L024977/1) and the ISIS Neutron and Muon Source for beamtime (RB1210310).

References

1 D. S. Jeong, R. Thomas, R. S. Katiyar, J. F. Scott, H. Kohlstedt, A. Petraru and C. S. Hwang, *Rep. Prog. Phys.*, 2012, **75**, 076502.
2 K. Singh, J. Nowotny and V. Thangadurai, *Chem. Soc. Rev.*, 2013, **42**, 1961–1972.
3 S. Zhang, F. Li, X. Jiang, J. Kim, J. Luo and X. Geng, *Prog. Mater. Sci.*, 2015, **68**, 1–66.
4 Z. M. Wang, B. Zhang, T. Otsuka, K. Inoue, H. Kobayashi and M. Kurmoo, *Dalton Trans.*, 2004, 2209–2216.
5 P. Jain, N. S. Dalal, B. H. Toby, H. W. Kroto and A. K. Cheetham, *J. Am. Chem. Soc.*, 2008, **130**, 10450.
6 X.-Y. Wang, Z.-M. Wang and S. Gao, *Chem. Commun.*, 2008, 281–294.
7 M. Sanchez-Andujar, L. C. Gomez-Aguirre, B. P. Doldan, S. Yanez-Vilar, R. Artiaga, A. L. Llamas-Saiz, R. S. Manna, F. Schnelle, M. Lang, F. Ritter, A. A. Haghighirad and M. A. Senaris-Rodriguez, *Crystengcomm*, 2014, **16**, 3558–3566.
8 Z. Wang, B. Zhang, K. Inoue, H. Fujiwara, T. Otsuka, H. Kobayashi and M. Kurmoo, *Inorg. Chem.*, 2007, **46**, 437–445.
9 M. Kurmoo, K.-L. Hu, Z. Wang and S. Gao, *Chem. Eur. J.*, 2009, **15**, 12050–12064.
10 B.-Q. Wang, H.-B. Yan, Z.-Q. Huang and Z. Zhang, *Acta Cryst. C*, 2013, **69**, 616.
11 X. Y. Wang, L. Gan, S. W. Zhang and S. Gao, *Inorg. Chem.*, 2004, **43**, 4615–4625.
12 P. Jain, V. Ramachandran, R. J. Clark, H. D. Zhou, B. H. Toby, N. S. Dalal, H. W. Kroto and A. K. Cheetham, *J. Am. Chem. Soc.*, 2009, **131**, 13625.
13 W. Wang, L. Q. Yan, J. Z. Cong, Y. L. Zhao, F. Wang, S. P. Shen, T. Zou, D. Zhang, S. G. Wang, X. F. Han and Y. Sun, *Sci. Rep.*, 2013, **3**, 2024.
14 R. I. Thomson, P. Jain, A. K. Cheetham and M. A. Carpenter, *Phys. Rev. B*, 2012, **86**, 214304.
15 M. Sanchez-Andujar, S. Presedo, S. Yanez-Vilar, S. Castro-Garcia, J. Shamir and M. A. Senaris-Rodriguez, *Inorg. Chem.*, 2010, **49**, 1510–1516.
16 D.-W. Fu, W. Zhang, H.-L. Cai, Y. Zhang, J.-Z. Ge, R.-G. Xiong, S. D. Huang and T. Nakamura, *Angew. Chem. Int. Ed.*, 2011, **50**, 11947–11951.
17 M. Maczka, A. Gagor, B. Macalik, A. Pikul, M. Ptak and J. Hanuza, *Inorg. Chem.*, 2014, **53**, 457–467.
18 T. Besara, P. Jain, N. S. Dalal, P. L. Kuhns, A. P. Reyes, H. W. Kroto and A. K. Cheetham, *Proc. Nat. Acad. Sci.*, 2011, **108**, 6828–6832.
19 T. Asaji, S. Yoshitake, Y. Ito and H. Fujimori, *J. Mol. Struct.*, 2014, **1076**, 719–723.
20 M. T. Dove, M. G. Tucker and D. A. Keen, *Eur. J. Mineral.*, 2002, **14**, 331–348.
21 H. M. Rietveld, *J. Appl. Cryst.*, 1969, **2**, 65 – 71.
22 A. C. Larson and R. B. Von Dreele, *General Structure Analysis System (GSAS)*, Los Alamos National Laboratory Technical Report LAUR 86-748, 2004.
23 B. H. Toby, *J. Appl. Cryst.*, 2001, **34**, 210–213.
24 M. G. Tucker, D. A. Keen, M. T. Dove, A. L. Goodwin and Q. Hui, *J. Phys. Cond. Matt.*, 2007, **19**, 335218.
25 J. Schlenker, G. Gibbs and M. Boisen, *Acta Cryst. A*, 1978, **34**, 52–54.
26 V. M. Nield and D. A. Keen, *Diffuse Neutron Scattering from Crystalline Materials*, Clarendon Press, 2001.
27 T. Steiner, *Angew. Chem. Int. Ed.*, 2002, **41**, 48–76.
28 C. L. Perrin and J. B. Nielson, *Ann. Rev. Phys. Chem.*, 1997, **48**, 511–544.

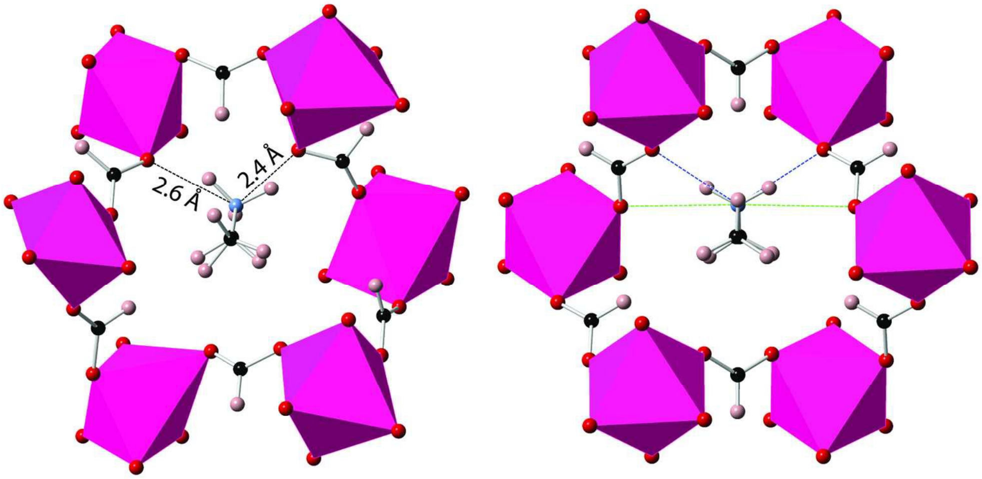
2.6 Å
2.4 Å